Analysis and Utilization of the Frequency Splitting Phenomenon in Wireless Power Transfer Systems

Xu Liu, Xibo Yuan, *Senior Member, IEEE*, Chenyang Xia, and Xiaojie Wu

***Abstract*—The frequency splitting phenomenon (FSP) is a critical issue in wireless power transfer (WPT) systems. When the FSP exists, the load power will sharply increase and can be dozens of times of the power obtained at the resonant frequency if the driving frequency varies from the resonant frequency, which seriously affects the system safety. This article studies the impacts caused by the FSP in detail and then proposes a system control method by utilizing the advantages of the FSP to realize constant power output and zero voltage switching (ZVS) of the dc–ac inverter simultaneously. The splitting frequencies are tracked and the driving frequency is precisely adjusted together with the dc-link voltage. The specific implementation method is given in this article to minimize the impacts on the power transfer performance. An 85 kHz, 3.3 kW WPT system is built up to validate the proposed method. The experimental results show that when the FSP occurs at 150 mm coil-to-coil distance and 5 Ω load resistance, the load power can be hold at 3.3 kW with the dc-link voltage reduced from 327 to 160 V. Meanwhile, ZVS of the inverter is realized and the inverter efficiency is improved from 95% to 97%.**

***Index Terms*—Frequency splitting phenomenon (FSP), output power control, wireless power transfer (WPT), zero voltage switching (ZVS).**

I. Introduction

WIRELESS power transfer (WPT) technology can transfer electric energy from a power source to a load across an air gap without direct electrical contacts. It is attracting more and more attention and has been widely used in implantable devices [1]–[4], electric vehicles [5]–[8], and portable devices [9], [10] to power up or recharge the battery of an electric equipment. Due to the elimination of physical contacts between the source and the load, WPT systems can greatly enhance the flexibility and safety of the electrical equipment.

A common WPT system is composed of a transmitting coil and a receiving coil. The electrical energy can be wirelessly transferred through the air gap by the mutual inductance of these two coils, while the leakage inductance which is only associated with one coil does not have a direct contribution to the active power transfer [11]. When the distance between the two coils is larger than a critical value and if the mutual inductance is too large, the characteristics of the transferred power will change from a single peak curve to a double peak curve when the driving frequency moves away from the resonant frequency. This is called the frequency splitting phenomenon (FSP) [12]. In a practical WPT system, the driving frequency is almost impossible to be exactly the same as the resonant frequency due to, e.g., the errors in the measurement of the inductance of the coils and the capacitance of the compensation capacitors, or the self-inductance changes caused by the variation of the relative positions between the two coils when ferrite is added in the coils. Consequently, a lot of research efforts have been directed toward optimizing the system performance by suppressing the frequency splitting effect, as the FSP is a key issue related to the power transfer efficiency, amount and safety of the WPT systems.

In [12], the splitting frequency equation is defined and a zero-phase control method is presented to track the splitting frequency when the coupling changes in the splitting region. In this way, the load voltage can be maintained when the coupling coefficient changes. The coupled model theory is adopted in [13] and the FSP is studied in two, three, and four coils systems, respectively. The results show that the FSP exists in each WPT system. In a two-coil system, there are two frequency splitting points, while in a multicoil system, there will be more frequency splitting points. Circuit analysis methods on the FSP in the two, three, and four coils WPT systems can be respectively found in [14]–[16]. Similar results have been obtained as the coupled model theory. Meanwhile, the efficiency of the WPT system is also studied in [14] and the results show that the FSP only occurs on the load power characteristics, while the efficiency curve does not split corresponding to the driving frequency in the two-coil system. Apart from these studies on various number of coils, many other studies are also carried out on compensation topologies of the WPT system. In [17] and [18], the four basic compensation topologies of the WPT system [series–series (SS), parallel–parallel (PP), parallel–series (PS), series–parallel (SP)] are all studied for the FSP. It has been found that with the increase in the coupling coefficient, the WPT systems with SS and SP compensation topologies both show FSP. However, in the other two systems, the FSP does not appear.

As the SS compensation topology is most widely used in the WPT systems, many works have been carried out to suppress

Manuscript received May 11, 2020; revised August 10, 2020; accepted September 11, 2020. Date of publication September 21, 2020; date of current version November 20, 2020. This work was supported by the Fundamental Research Funds for the Central Universities under Project 2019QNA08. Recommended for publication by Associate Editor R. Zane. *(Corresponding author: Xibo Yuan.)*

Xu Liu, Chenyang Xia, and Xiaojie Wu are with the Jiangsu Province Laboratory of Mining Electric and Automation, China University of Mining and Technology, Xuzhou 221116, China (e-mail: xu.liu@cumt.edu.cn; bluesky198210@163.com; zgcumt@126.com).

Xibo Yuan is with the Department of Electrical and Electronic Engineering, University of Bristol, Bristol BS8 1UB, U.K. (e-mail: xibo.yuan@bristol.ac.uk).

Color versions of one or more of the figures in this article are available online at https://ieeexplore.ieee.org.

Digital Object Identifier 10.1109/TPEL.2020.3025480

the FSP in it. A method of using nonidentical resonant coils is presented in [19] to eliminate the FSP. It is found that when the transmitting coil is large enough compared to the receiving coil, the FSP can be eliminated. Another method is proposed in [20] by adjusting the load resistor to suppress the FSP. The results show that when the FSP occurs, increasing the load resistance can help to suppress the frequency splitting. The frequency splitting elimination method in a four-coil WPT system is studied in [21]. It is found that reducing the source internal resistance, and increasing the mutual inductance of the source coil and the transmitting coil, as well as the mutual inductance of the load coil and the receiving coil, all help relieve the FSP and improve the efficiency. However, in a practical WPT system, the size of the coils and the position of the coils are usually fixed, the internal resistance of the power source and the load resistance are also fixed. Therefore, the FSP is very difficult to be totally eliminated in practice. As a consequence, there should be more works carried out to find the advantages and disadvantages of the FSP in the WPT systems. For example, Narayanamoorthi *et al.* in [22] try to utilize the FSP to transfer power and information simultaneously.

In this article, the FSP is analyzed in detail not only on the power transfer amount and efficiency, but also on the characteristics of the reflected impendence from the secondary side to the primary side, the characteristics of the input impendence of the dc–ac inverter and the primary and secondary sides efficiencies. It is found out in this article that when the FSP occurs, adjusting the driving frequency to the splitting frequency can achieve maximum load power, and therefore decrease the dc input voltage with the same load power obtained at the resonant frequency. Meanwhile, adjusting the characteristic of the input impendence of the system by tuning the driving frequency can also help to realize zero voltage switching (ZVS) of the dc–ac inverter. Based on the theoretical analysis, a detailed implementation method by utilizing the FSP to hold the load power constant and realize ZVS of the dc–ac inverter simultaneously under a varied load resistance or coupling coefficient is presented. The experimental results show when the coupling coefficient or the load resistance varies, the load power can be hold constant at the maximum output power point with a much lower dc input voltage, which can reduce the voltage stress of the components used in the WPT system. Meanwhile, ZVS of the dc–ac inverter can be realized and the inverter efficiency can be effectively improved to provide a more reliable operating condition for the inverter.

The rest of this article is organized as follows. The impacts of the FSP on the power transfer amount, efficiency, characteristics of the reflected impendence from the secondary side to the primary side, characteristics of the input impendence of the dc–ac inverter of the two-coil SS-compensated WPT system are studied in Section II. Meanwhile, the inverter operation modes are also discussed when the driving frequency varies from the resonant frequency. Based on the theoretical analysis, the implementation methods of the constant output power control strategy and the ZVS implementation strategy of the dc–ac inverter by utilizing the FSP are given in Section III. The correctness of the analysis and the effectiveness of the proposed strategies is experimentally validated on an 85 kHz, 3.3 kW WPT system and the results are given in Section IV. Finally, Section V concludes the article.

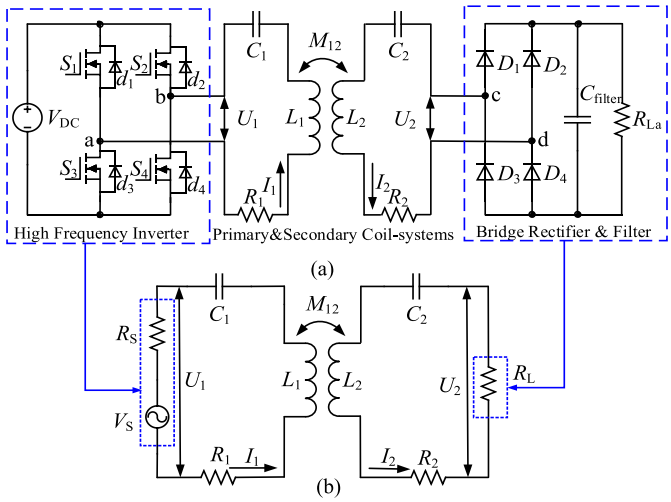

Fig. 1. WPT system. (a) Whole system. (b) Simplified model.

II. Theoretical Analysis of the FSP

The typical circuit diagram of the WPT system is shown in Fig. 1(a). The primary-side system consists of the transmitting coil L_1 and its series-connected compensation capacitor C_1. It is driven by a high-frequency voltage-source inverter. At the secondary side, the compensation capacitor C_2 is also series connected with the receiving coil L_2, and then the received power is delivered to the load through a passive rectifier. At the primary and secondary sides, the compensation capacitors are both set to resonant with the coils, which means the resonant angular frequency $\omega_r = 1/\sqrt{L_1C_1} = 1/\sqrt{L_2C_2}$ [23]. The WPT system shown in Fig. 1(a) can be simplified into the equivalent simplified model, as shown in Fig. 1(b). The rectifier, filter capacitor, and the actual load $R_{\rm La}$ are modeled as an equivalent resistance $R_{\rm L}$

$$R_L = \left(\frac{2\sqrt{2}}{\pi}\right)^2 R_{La}. \tag{1}$$

With the lumped-element circuit shown in Fig. 1(b), the current vectors of the primary and secondary sides ($\boldsymbol{I_1}$ and $\boldsymbol{I_2}$) can be derived, respectively, according to the Kirchhoff voltage law as follows:

$$\overrightarrow{I_1} = \frac{Z_2\overrightarrow{U_1}}{\omega_d^2 M_{12}^2 + Z_1 Z_2} \tag{2}$$

$$\overrightarrow{I_2} = \frac{j\omega_d M_{12}\overrightarrow{U_1}}{\omega_d^2 M_{12}^2 + Z_1 Z_2} \tag{3}$$

where $Z_1 = R_1 + j\omega_d L_1 - j/(\omega_d C_1)$ is the impedance of the primary side; $Z_2 = R_L + R_2 + j\omega_d L_2 - j/(\omega_d C_2)$ is the impedance of the secondary side; and ω_d is the driving angular frequency.

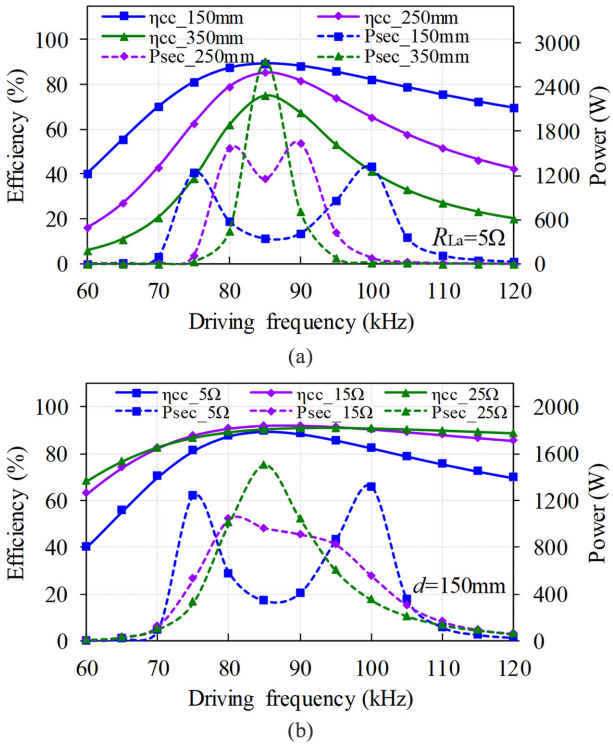

Fig. 2. Effect of driving frequency on the WPT system performance. (a) Fixed load resistance and varied coil-to-coil distances. (b) Fixed coil-to-coil distance and varied load resistances.

With (2) and (3), the power injected into the primary-side coil system, $P_{\rm pri}$, the power received by the secondary-side coil system, $P_{\rm sec}$, and accordingly, the coil-to-coil efficiency, η_{cc} then can be expressed as follows:

$$P_{\rm pri} = \overrightarrow{U_1}\overrightarrow{I_1} = U_1 I_1 \cos\phi \tag{4}$$

$$P_{\rm sec} = \overrightarrow{I_2}^2 R_L = I_2^2 R_L \tag{5}$$

$$\eta_{cc} = \frac{P_{\rm sec}}{P_{\rm pri}} \tag{6}$$

$$\cos\phi = \frac{\text{real}\,(Z_{\rm in})}{|Z_{\rm in}|} \tag{7}$$

$$Z_{\rm in} = \frac{\overrightarrow{U_1}}{\overrightarrow{I_1}} = Z_1 + \frac{\omega_d^2 M_{12}^2}{Z_2} \tag{8}$$

where ϕ is the phase angle between the voltage $\boldsymbol{U_1}$ and the current $\boldsymbol{I_1}$, and $Z_{\rm in}$ is the input impedance of the inverter.

From (2)–(8), it can be found that for a given WPT system, $P_{\rm pri}$, $P_{\rm sec}$, and $\eta_{\rm cc}$ are all closely related to the driving frequency, the load resistance, and the mutual inductance between the two coils.

Fig. 2 illustrates the impacts of driving frequency on the WPT system performance under various conditions. In this article, the self-inductance of the transmitting and receiving coils are both 65 μH and the resonant frequency is set to be 85 kHz. The vertical coil-to-coil distance is set at 150, 250, and 350 mm,

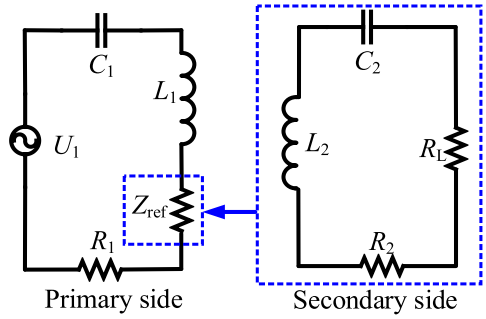

Fig. 3. Separated WPT system circuit model.

which are the typical vehicle chassis heights and accordingly result in the coupling coefficient to be 0.28, 0.15, and 0.09. The load resistance is set at 5, 15, and 25 Ω to provide different load conditions. The dc input voltage is kept constant at 100 V.

It can be seen from Fig. 2 that the FSP would occur when the coil-to-coil distance is so short that the coupling coefficient is greater than the critical value [see Fig. 2(a)], or the load resistance is low enough [see Fig. 2(b)]. As such, the maximum output power now can be found at another two driving frequencies which are on each side of the resonant frequency with slightly less efficiency than the efficiency at the resonant frequency. It also shows that when the FSP disappears, with an increase in the driving frequency, the peak output power is found at the resonant frequency, and the output power decreases rapidly when the driving frequency is away from the resonant frequency.

To further illustrate the influence of frequency splitting on the system, the simplified WPT model circuit [see Fig. 1(b)] can be separated into two parts, namely, the primary side and the secondary side, as shown in Fig. 3.

In this model, the secondary side can be treated as a reflected impedance ($Z_{\rm ref}$) in the primary side. Accordingly, the secondary-side efficiency $\eta_{\rm sec}$, the primary-side efficiency $\eta_{\rm pri}$, and the coil-to-coil efficiency η_{cc} can be calculated as follows:

$$\eta_{\rm sec} = \frac{R_L}{R_L + R_2} \tag{9}$$

$$\eta_{\rm pri} = \frac{\text{real}\,(Z_{\rm ref})}{\text{real}\,(Z_{\rm ref}) + R_1} \tag{10}$$

$$\eta_{cc} = \eta_{\rm sec} \times \eta_{\rm pri} \tag{11}$$

$$Z_{\rm ref} = \frac{(\omega_d M_{12})^2}{Z_2}. \tag{12}$$

Equations (9)–(12) indicate that changing the driving frequency will not change the efficiency of the secondary side, but will affect the primary side as the reflected impedance from the secondary side will change with the driving frequency.

The real part of the reflected impedance Real($Z_{\rm ref}$) and the primary side efficiency $\eta_{\rm pri}$ under different conditions are plotted in Figs. 4 and 5, respectively. It can be seen that with an increase in the load resistance, the driving frequencies corresponding to the maximum Real($Z_{\rm ref}$) in Fig. 4(a) and to the maximum

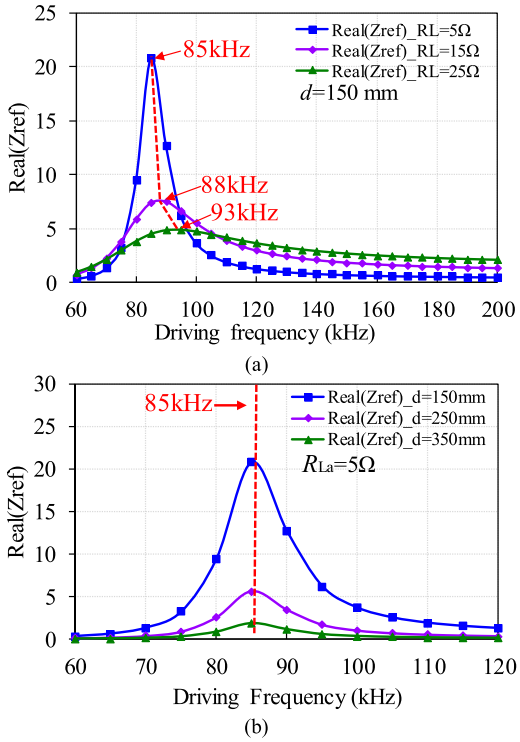

Fig. 4. Effect of driving frequency on the real part of the reflected impedance. (a) Fixed coil-to-coil distance and varied load resistance. (b) Fixed load resistance and varied coil-to-coil distance.

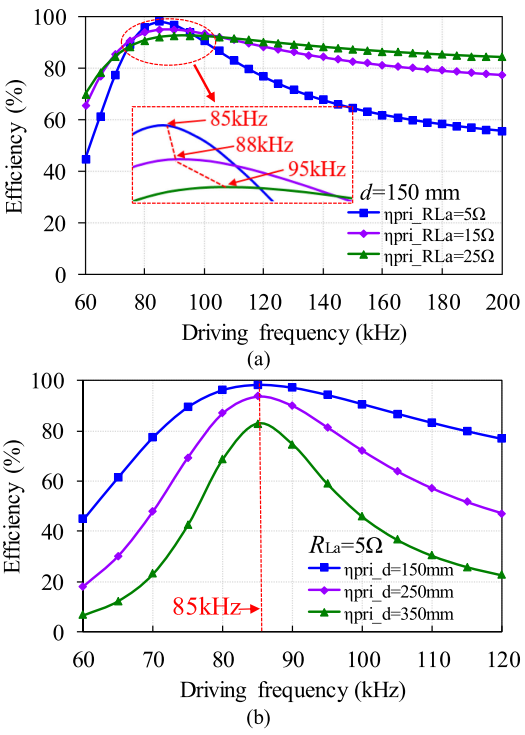

Fig. 5. Effect of driving frequency on the primary side efficiency. (a) Fixed coil-to-coil distance and varied load resistance. (b) Fixed load resistance and varied coil-to-coil distance.

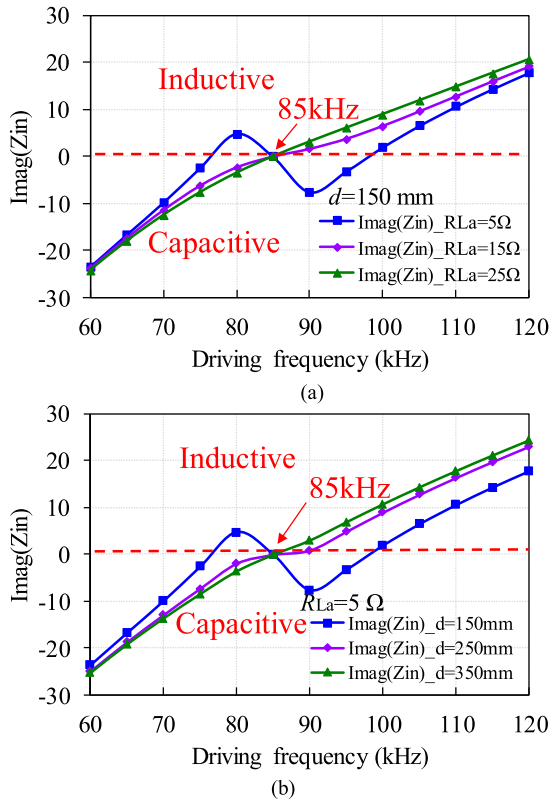

Fig. 6. Effect of driving frequency on the imaginary part of the input impedance. (a) Fixed coil-to-coil distance and varied load resistance. (b) Fixed load resistance and varied coil-to-coil distance.

η_{pri} in Fig. 5(a) will increase and have the same values, i.e., 85 kHz with 5 Ω load, 88 kHz with 15 Ω load, and 95 kHz with 25 Ω load. Besides, it can also be seen from Figs. 4 and 5 that the smaller the load resistance is, the closer the frequencies corresponding to the maximum Real(Z_{ref}) and to the maximum η_{pri} are to the resonant frequency. Meanwhile, when the driving frequency is higher than the resonant frequency, with the driving frequency continually increasing, it can be seen that the smaller the load resistance is, the rapidly the Real(Z_{ref}) and η_{pri} will be decreasing [see Fig. 5(a)]. When the load resistance is fixed, the driving frequency corresponding to the maximum Real(Z_{ref}) and η_{pri} will not be affected by the coupling coefficient [see Figs. 4(b) and 5(b)].

When the driving frequency varies from the resonant frequency, there will be a phase angle between the output voltage and current of the inverter. The characteristic of the input impedance reflects the apparent output power of the inverter and the phase relationship between the output voltage and current of the inverter. Fig. 6 plots the imaginary part of the input impedance of the inverter when the driving frequency f_{d} is swept around the resonant frequency f_{r}. It can be seen from Fig. 6(a) that when the load resistance is 5 Ω (blue curve), the input impedance is inductive when f_{d} is between 76 and 85 kHz or greater than 98 kHz, and is capacitive when f_{d} is between 85 and 98 kHz or smaller than 76 kHz. When the load

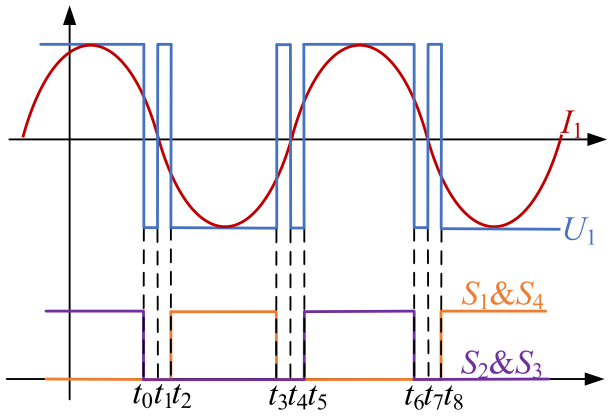

Fig. 7. Waveforms of $\boldsymbol{U_1}$ and $\boldsymbol{I_1}$ and gate signals of the inverter with $f_\mathrm{d} = f_\mathrm{r}$.

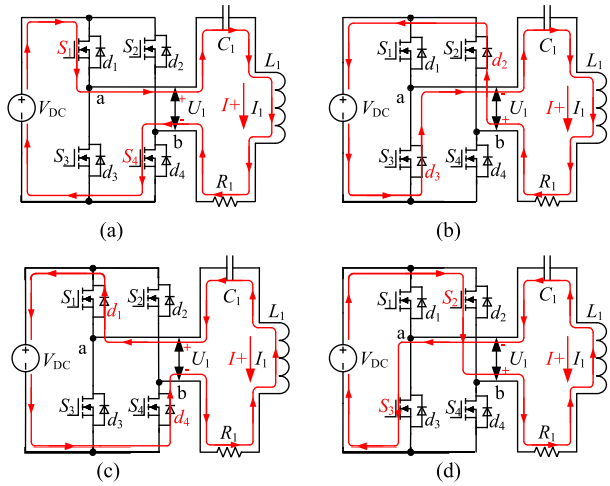

Fig. 8. Operation modes of the inverter in a full switching cycle with $f_\mathrm{d} = f_\mathrm{r}$. (a) Before t_0. (b) t_0–t_1. (c) t_1–t_2. (d) t_2–t_5.

resistance is 15 or 25 Ω (purple curve and green curve), the input impedance is always inductive when f_d is greater than 85 kHz, and is always capacitive when f_d is smaller than 85 kHz. With regards to Fig. 6(b), similar results can be derived, as in Fig. 6(a). As a result, when the FSP occurs (blue curve), an increase in f_d (initial $f_\mathrm{d} << f_\mathrm{r}$) will make the input impedance first capacitive and then inductive until $f_\mathrm{d} = f_\mathrm{r}$, whereas a reduction in f_d (initial $f_\mathrm{d} >> f_\mathrm{r}$) will produce a first inductive and then a capacitive input impedance until $f_\mathrm{d} = f_\mathrm{r}$. The changing points of the characteristic of Z_in correspond to the frequency splitting points. When the FSP is suppressed (as shown in purple and green curves), increasing the driving frequency from the resonant frequency will always lead to an inductive input impedance and decreasing the driving frequency from the resonant frequency will always lead to a capacitive input impedance.

Varying the driving frequency will change the characteristic of the input impendence, while the input impendence is closely related to the operation modes of the dc–ac inverter. Therefore, the analysis on the operation modes of the dc–ac inverter in the WPT system is a non-negligible problem when the driving frequency varies from the resonant frequency.

In order to find out the operation characteristic of the inverter in the WPT system when the driving frequency varies, the inverter operation mode in the resonant condition should be analyzed first. It has been analyzed that when the system operates in resonant condition, the output voltage of the inverter $\boldsymbol{U_1}$ and the output current of the inverter $\boldsymbol{I_1}$ are in phase. With regards to the full bridge inverter used in this article, as shown in Fig. 1(a), a dead-time must be added right after one switch turns OFF and before its complementary switch turns ON to avoid shoot-through and guarantee safe operation of the inverter. As a result, $\boldsymbol{I_1}$ cannot cross zero exactly when the MOSFETs are turned ON or OFF, which will produce switching losses. In a practical WPT system, the output voltage and current waveforms of the dc–ac inverter are shown in Fig. 7.

The detailed operation modes of the inverter in the resonant WPT system from t_0–t_5 are shown in Fig. 8 and explained below. The initial state of the inverter output voltage and current ($I+$) are defined to be the reference direction.

Before $\boldsymbol{t_0}$: S_1 and S_4 are turned ON and S_2 and S_3 are turned OFF. $\boldsymbol{U_1}$ and $\boldsymbol{I_1}$ are both positive but $\boldsymbol{I_1}$ has started to decrease, as L_1 is discharging in the LC resonant circuit.

$\boldsymbol{t_0}$–$\boldsymbol{t_1}$: S_1 and S_4 are turned OFF, the body diodes of S_2 and S_3, d_2 and d_3, are ON and the system operates in dead-time. $\boldsymbol{U_1}$ is negative but $\boldsymbol{I_1}$ is still positive because the discharging inductor L_1 is charging the capacitor C_1 and $\boldsymbol{I_1}$ keeps decreasing. S_1 and S_4 are hard switching OFF.

$\boldsymbol{t_1}$–$\boldsymbol{t_2}$: Four MOSFETs are all turned OFF, the system still operates in dead-time. At t_1, L_1 finishes its discharging process and C_1 starts to discharge because of the resonant LC circuit. Therefore, $\boldsymbol{I_1}$ is negative after crossing zero and $\boldsymbol{U_1}$ is positive, and d_1 and d_4 are ON.

$\boldsymbol{t_2}$–$\boldsymbol{t_5}$: S_1 and S_4 remain OFF and S_2 and S_3 are turned ON at t_2. $\boldsymbol{U_1}$ and $\boldsymbol{I_1}$ are both negative but $\boldsymbol{I_1}$ will decrease when the capacitor C_1 is fully discharged and repeat the process from t_0–t_2 with opposite direction of output voltage and current. S_2 and S_3 are hard switching ON.

The driving frequency varies from the resonant frequency and results in a capacitive input impendence of the inverter, and the zero-current point of $\boldsymbol{I_1}$ occurs before t_0 (see Fig. 7). The waveforms of $\boldsymbol{U_1}$ and $\boldsymbol{I_1}$ and gate signals of the inverter will be shown as Fig. 9. At t_0, $\boldsymbol{I_1}$ crosses zero and S_1 and S_4 are kept switched ON to conduct the current, but the direction of $\boldsymbol{I_1}$ is reversed. At t_1, S_2 and S_3 remain OFF, and S_1 and S_4 are switched OFF. $\boldsymbol{U_1}$ and $\boldsymbol{I_1}$ both keep their direction, the current diverts from the channel of S_1 and S_4 into their body diodes d_1 and d_4, creating ZVS OFF for S_1 and S_4. At $\boldsymbol{t_2}$, S_2 and S_3 are switching ON and $\boldsymbol{I_1}$ flows through S_2 and S_3, meanwhile, d_1 and d_4 are OFF, and $\boldsymbol{U_1}$ will be zero immediately. Therefore, at t_2, S_2 and S_3 are hard switching ON.

The input impendence of the inverter appears as inductive and the zero-current point of $\boldsymbol{I_1}$ will be shifted out of the dead-time after t_2 (see Fig. 7). The output voltage and current waveforms of the inverter will be shown as Fig. 10. Because of the inductive impedance of the inverter, the current lags the voltage. Therefore,

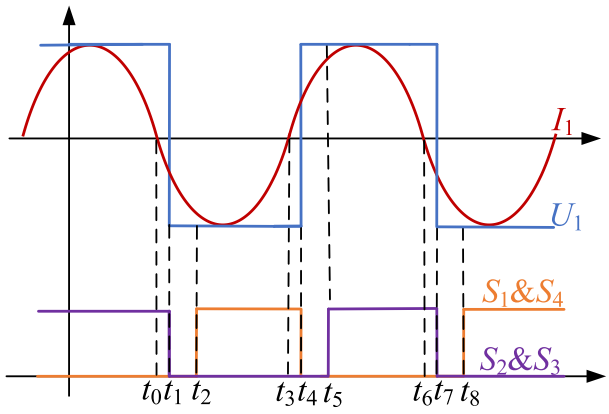

Fig. 9. Waveforms of $\boldsymbol{U_1}$ and $\boldsymbol{I_1}$ and gate signals of the inverter with capacitive input impendence.

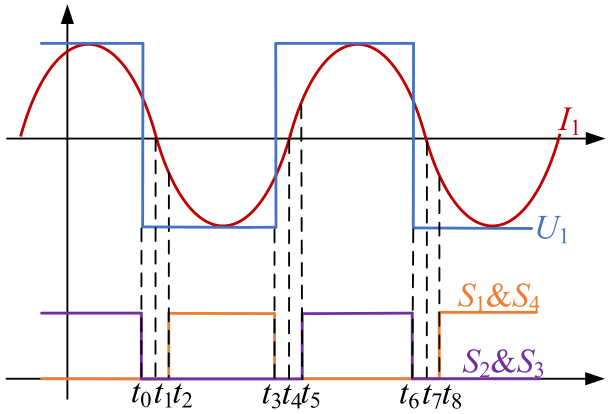

Fig. 10. Waveforms of $\boldsymbol{U_1}$ and $\boldsymbol{I_1}$ and gate signals of the inverter with inductive input impendence.

when $\boldsymbol{U_1}$ crosses zero at t_0, $\boldsymbol{I_1}$ will be still positive but decreasing and cross zero at t_1 and then be negative. At t_2, S_2 and S_3 are switching ON, the current is diverting from their respective body diodes to their channels, therefore, S_2 and S_3 are ZVS ON. During t_2 to t_3, S_1 and S_4 are OFF and S_2 and S_3 are turned ON. $\boldsymbol{U_1}$ and $\boldsymbol{I_1}$ are both negative and $\boldsymbol{I_1}$ will increase first and then decrease because of the *LC* circuit. $\boldsymbol{I_1}$ will lag $\boldsymbol{U_1}$ in crossing zero because of the inductive impedance. Therefore, at t_3, S_2 and S_3 are hard switching OFF.

From the above analysis, it is obvious that when the WPT system operates at resonant condition, all the four switching devices in the full bridge inverter are in hard switching ON and OFF. Besides, it can be found that the switching transient always happen in the dead-time and the hard switching of the switching devices is caused by the *LC* circuit operating in resonant condition and appearing pure resistive. While when the driving frequency varies from the resonant frequency and results in inductive or capacitive input impendence of the inverter, and the zero-crossing point of $\boldsymbol{I_1}$ can be shifted out from the dead-time, only one pair of the body diodes of the MOSFET is conducting during the dead-time. Therefore, the MOSFETs in the full bridge inverter can achieve ZVS ON or OFF according to the impedance of the inverter. Besides, when the phase between $\boldsymbol{U_1}$ and $\boldsymbol{I_1}$ is shifted to remove the period of t_0–t_1 or t_1–t_2, the pulses during the dead-time can also be eliminated, which can help to reduce the stress on the switching devices.

Considering the conclusions derived in the theoretical analysis about the FSP, it can not only help to determine the optimal driving frequency to track the maximum output power, but also help to achieve ZVS ON or OFF of the full bridge dc–ac inverter as the driving frequency is bound to vary from the resonant frequency to trigger the FSP. Therefore, for a given system with specific requirement on the output power, the dc input voltage can be greatly reduced by tuning the driving frequency to the splitting frequencies, which can help to reduce the voltage stress on the switching devices and the compensation capacitors. Meanwhile, when the driving frequency is carefully designed to shift the zero-current point of $\boldsymbol{I_1}$ out of the dead-time, ZVS ON or OFF can also be realized, and the losses of the inverter can thereby be reduced.

III. Implementation Methods

A. Implementation Method of Output Power Control

It can be found out from (3) and (5) that for a given WPT system, tuning the dc input power is the most convenience way to achieve a constant output power when the load resistance or the mutual inductance varies. However, utilizing the FSP can not only help to control the output power, but also contribute to other performance improvements for the WPT system as analyzed in Section II. Therefore, these two methods will be compared in this article to find the advantages of the utilizing the FSP to control the output power. In the following sections, tuning the dc input voltage directly is named Method A, and utilizing the FSP to tune the output power is named Method B.

For method A, a variable regulated dc power supply is used, allowing the input voltage to be set at the desired value. The output power is proportional to the load resistance and the dc input voltage according to the secondary-side power expression given in (5). Assuming zero dead-time, the rms value of the fundamental component of a square wave is $2\sqrt{2}/\pi$ of the amplitude of the square wave as (13), then the relationship between the input dc voltage, output power, and load resistance can be derived as (14)

$$\left(2\sqrt{2}\Big/\pi\right) U_{\mathrm{DC}} = U_{1\mathrm{RMS}} \tag{13}$$

$$\overrightarrow{U_1} = \frac{\sqrt{P_{\mathrm{sec}}/R_L}\left(\omega_d^2 M_{12}^2 + Z_1 Z_2\right)}{j\omega_d M_{12}}. \tag{14}$$

In order to track the maximum output power, the frequencies corresponding to the frequency splitting points need to be derived first. The load power given in (5) is closely related to its partial derivative with respect to the driving frequency. The partial derivative with respect to the system driving frequency of the output power in the secondary side can be derived by

$$f_{(f_d)} = \frac{\partial P_{\mathrm{sec}}}{\partial f_d} = 0. \tag{15}$$

Therefore, the dc input voltage can be adjusted according by (16) to achieve the desired output power

$$\overrightarrow{U_1} = \frac{\sqrt{P_{\rm sec}/R_L}\left(\left(2\pi f_{\rm Ridge}\right)^2 M_{12}^2 + Z_1 Z_2\right)}{j2\pi f_{\rm Ridge} M_{12}}. \tag{16}$$

As can be seen from Fig. 2, when the FSP occurs, (15) will have three solutions, that is, $f_{\rm Ridege+}$, $f_{\rm Ridege-}$, and $f_{\rm Trough}$. The first two values are the two peak values on either side of the resonance frequency point. $f_{\rm Trough}$ corresponds to the trough value of the output power wave and equals the resonant frequency of the system. Therefore, the driving frequency can be converted to $f_{\rm Ridege+}$ or $f_{\rm Ridege-}$ to achieve the maximum power transfer capacity. The lower driving frequency can reduce the switching losses in the inverter and rectifier. Therefore, in this case, $f_{\rm Ridege-}$ is selected to be the tuning objective of the driving frequency. It should be noticed that when (15) has only one solution, the FSP disappears, and the output power attains its peak at the resonant frequency. In this case, adjusting the output power to the desired value only needs to directly tune the dc input voltage.

B. Implementation Method of ZVS Operation

It has been analyzed in Section II that in order to realize ZVS operation of the dc–ac inverter, the input impedance characteristic of the inverter needs to be turned into inductive or capacitive by tuning the driving frequency, and the zero-crossing point of $\boldsymbol{I_1}$ should be exactly shifted out of the dead-time to reduce the impacts on the power transfer amount and efficiency. Therefore, the phase difference of $\boldsymbol{U_1}$ and $\boldsymbol{I_1}$ should satisfy the following equations first:

$$\phi > \frac{2\pi\,(t/2)}{T} \tag{17}$$

$$\cos\phi < \cos\left(\frac{2\pi\,(t/2)}{T}\right) \tag{18}$$

where t is the dead-time and T is the period of the inverter output voltage. It means that the delay time between $\boldsymbol{U_1}$ and $\boldsymbol{I_1}$ is larger than a half of the dead-time.

The phase difference ϕ is also the phase angle of the input impedance of the inverter $Z_{\rm in}$ in (19). Equations (20) and (21) are, respectively, the real part and the imaginary part of $Z_{\rm in}$

$$Z_{in} = \frac{\overrightarrow{U_1}}{\overrightarrow{I_1}} = Z_1 + \frac{\omega_d^2 M_{12}^2}{Z_2} = R + jX \tag{19}$$

$$R = R_1 + \frac{\omega_d^2 M_{12}^2\,(R_2 + R_L)}{\left(R_2 + R_L\right)^2 + \left(\omega_d L_2 - 1/(\omega_d C_2)\right)^2} \tag{20}$$

$$X = \omega_d L_1 - \frac{1}{\omega_d C_1} - \frac{\omega_d^2 M_{12}^2\left(\omega_d L_2 - 1/(\omega_d C_2)\right)}{\left(R_2 + R_L\right)^2 + \left(\omega_d L_2 - 1/(\omega_d C_2)\right)^2}. \tag{21}$$

Therefore, the driving frequencies which can make the delay time between $\boldsymbol{U_1}$ and $\boldsymbol{I_1}$ larger than a half of the dead-time can be derived from (22) by linking (18) and (19)

$$\cos\phi = \frac{R}{|Z_{in}|} < \cos\left(\frac{2\pi\,(t/2)}{T}\right) = \alpha. \tag{22}$$

To simplify the calculation, R_1 and R_2 are assumed to be zero, then (20) and (21) can be transformed into the following equations:

$$R = \frac{\omega_d^2 M_{12}^2 R_L}{{R_L}^2 + \left(\omega_d L_2 - 1/(\omega_d C_2)\right)^2} \tag{23}$$

$$X = \omega_d L_1 - \frac{1}{\omega_d C_1} - \frac{\omega_d^2 M_{12}^2\left(\omega_d L_2 - 1/(\omega_d C_2)\right)}{{R_L}^2 + \left(\omega_d L_2 - 1/(\omega_d C_2)\right)^2}. \tag{24}$$

When the FSP does not exist, in order to minimize the impacts on the power transfer efficiency and amount, the driving frequency should be as close as possible to the resonant frequency when creating ZVS conditions and maintain the power transfer efficiency and amount simultaneously (see Figs. 2 and 6). Meanwhile, for the SS compensated WPT systems, the compensation capacitors are set to resonate with the coils, which means $\omega_r L_2 - 1/(\omega_r C_2) = 0$. Therefore, the value of $\omega_d L_2 - 1/(\omega_d C_2)$ in (23) and (24) will be very small compared to $R_{\rm L}$ in this case, and the following equation can be assumed to simplify the calculation:

$$\omega_d L_2 - 1/(\omega_d C_2) \approx 0. \tag{25}$$

With (25), (23) and (24) can be simplified to be as follows:

$$R = \frac{\omega_d^2 M_{12}^2}{R_L} \tag{26}$$

$$X = \omega_d L_1 - \frac{1}{\omega_d C_1}. \tag{27}$$

Therefore, in order to derive the critical driving frequencies, which can make the delay time between $\boldsymbol{U_1}$ and $\boldsymbol{I_1}$ exactly equal to a half of the dead-time, the following equation should be satisfied according to (22):

$$\cos\phi = \frac{R}{|Z_{\rm in}|} = \cos\left(\frac{2\pi\,(t/2)}{T}\right) = \alpha. \tag{28}$$

Substituting (26) and (27) into (28), the following can be derived:

$$\alpha = \frac{R}{|Z_{in}|} = \frac{\left(\frac{\omega_d^2 M_{12}^2}{R_L}\right)}{\sqrt{\left(\frac{\omega_d^2 M_{12}^2}{R_L}\right)^2 + \left(\omega_d L_1 - \frac{1}{\omega_d C_1}\right)^2}}. \tag{29}$$

Take the square of both sides of (29), the following can be obtained:

$$\alpha^2 = \frac{\left(\frac{\omega_d^2 M_{12}^2}{R_L}\right)^2}{\left(\frac{\omega_d^2 M_{12}^2}{R_L}\right)^2 + \left(\omega_d L_1 - \frac{1}{\omega_d C_1}\right)^2}. \tag{30}$$

It is assumed that

$$x = \omega_d^2. \tag{31}$$

Substituting (31) into (30), the following equation can be obtained:

$$\alpha^2 = \frac{\left(\frac{xM_{12}^2}{R_L}\right)^2}{\left(\frac{xM_{12}^2}{R_L}\right)^2 + \left(xL_1{}^2 + \frac{1}{xC_1{}^2} - 2\frac{L_1}{C_1}\right)}. \tag{32}$$

And then, (36) can be derived after the mathematical transformation of (32) as given from (33)–(35)

$$\alpha^2\left(\frac{xM_{12}^2}{R_L}\right)^2 + \alpha^2\left(xL_1{}^2 + \frac{1}{xC_1{}^2} - 2\frac{L_1}{C_1}\right) = \left(\frac{xM_{12}^2}{R_L}\right)^2 \tag{33}$$

$$(1-\alpha^2)\left(\frac{xM_{12}^2}{R_L}\right)^2 - \alpha^2\left(xL_1{}^2 + \frac{1}{xC_1{}^2} - 2\frac{L_1}{C_1}\right) = 0 \tag{34}$$

$$\frac{1-\alpha^2}{\alpha^2}\left(\frac{M_{12}^2}{R_L}\right)^2 x^2 - L_1{}^2 x - \frac{1}{C_1{}^2 x} + 2\frac{L_1}{C_1} = 0 \tag{35}$$

$$\left(\frac{1}{\alpha^2} - 1\right)\frac{M_{12}^4}{R_L^2}x^3 - L_1^2 x^2 + \frac{2L_1}{C_1}x - \frac{1}{C_1^2} = 0 \tag{36}$$

where $\alpha = \cos(2\pi(t/2)/T)$.

The desired driving frequencies can thereby be derived with (31) and (36), which are closely related to M_{12}, L_1, C_1, R_L, t, and T. For the cubic equation (36), three roots can be derived. Obviously, the desired driving frequency is a real and positive value. Besides, as there are two critical points of the dead-time range, there will be at least two driving frequencies that can shift zero-current point out of the dead-time. Therefore, meaningful driving frequencies can be derived from the mathematical calculation with the help of the mathematical calculation tool such as MATLAB when the related system parameters are substituted into (36). For example, when the FSP gradually disappears at a 15 Ω load and 150 mm coil-to-coil distance (see Figs. 2 and 6), the calculated driving frequencies are about 80 kHz, 91 kHz, and 1 MHz, respectively. However, in order to derive (36), the desired driving frequency should not be away from the resonant frequency too much as analyzed previously. Therefore, one of these three roots (1 MHz) is invalid as the assumption (25) is no longer valid and the omitting items in Z_in cannot be ignored anymore. Regarding the other two roots ($f_1 = 80$ kHz, $f_2 = 91$ kHz), these two roots mean that the tuned driving frequency can exactly shift the zero-crossing point of $\boldsymbol{I_1}$ out of the dead-time of $\boldsymbol{U_1}$. In other words, with the driving frequencies derived from (31) and (36), the zero-crossing point of $\boldsymbol{I_1}$ can be exactly moved from t_1 (resonant condition) to t_0 (f_1) or t_2 (f_2), as shown in Fig. 11, in theory. However, due to the assumptions made during the calculation process [see equations (23)–(25)], these roots are only approximate values. The calculated driving frequencies will be resubstituted into the full expression of (19)–(22) to validate (18) in MATLAB. If (18) is not valid, the calculated driving frequency will be finetuned up or down (1 kHz in this article). And, the final results are 78 and 95 kHz, respectively, when the load resistance is 15 Ω, which can satisfy (18) and tune the input impedance of the inverter into capacitive and inductive accordingly.

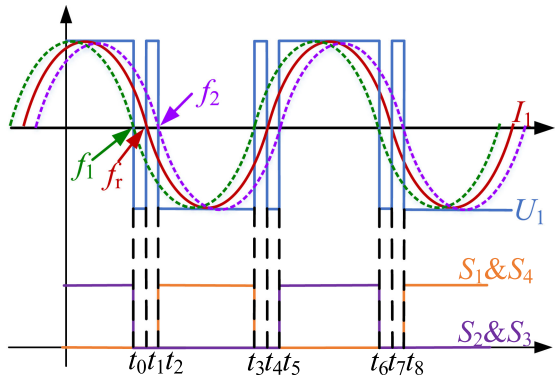

Fig. 11. Phase relationship between $\boldsymbol{U_1}$ and $\boldsymbol{I_1}$ with critical driving frequencies derived from the calculations.

When the FSP occurs, as can be seen from Figs. 2 and 6, the driving frequency only needs to be slightly higher or lower than the splitting frequencies to achieve ZVS ON or OFF (inductive or capacitive input impendence of the dc–ac inverter), and can maintain the output power around the extreme values, otherwise, the load power will be seriously affected. As lower the switching frequency can further reduce the switching losses, frequencies around $f_{\mathrm{Ridege}-}$ are selected to be the desired values. To make sure the zero-current point of $\boldsymbol{I_1}$ can be shifted out of the dead-time, the calculated driving frequency will be resubstituted into the full expressions of (19)–(22) to validate (18) in MATLAB. If (18) is not valid, the calculated driving frequency will be finetuned up or down, i.e., when ZVS ON is expected, the driving frequency will be tuned up from $f_{\mathrm{Ridege}-}$ to achieve inductive input impendence; when ZVS OFF is expected, the driving frequency will be tuned down from $f_{\mathrm{Ridege}-}$ to achieve capacitive input impendence. For example, when the load resistance is 5 Ω and the power transfer distance is 150 mm, the FSP occurs (see Figs. 2 and 6). The frequency splitting points can be derived from (15), which are 76 kHz ($f_{\mathrm{Ridege}-}$) and 98 kHz ($f_{\mathrm{Ridege}+}$), respectively. As analyzed above, frequencies around $f_{\mathrm{Ridege}-}$ will be selected as the desired driving frequencies, which will be finetuned up and down from 76 kHz and resubstituted into the full expression of (19)–(22) to validate (18). And the final results are 75 and 78 kHz, respectively, when the load resistance is 5 Ω, which can satisfy (18) and tune the input impedance of the inverter into capacitive and inductive accordingly.

IV. Experimental Results

For validating the theoretically analysis presented in this article about the FSP and its utilizing methods, an 85 kHz, 3.3 kW two-coil SS-compensated WPT system is built up, the detailed parameters of this setup are listed in Table I. The design of the transmitting coil is as same as the receiving coil as shown in Fig. 12, and the design parameters of the coils are listed in Table II. The detailed design and optimization method of these two coils can be found in our previous work [24], which can help to improve the power transfer efficiency and capacity simultaneously when the coil size is limited and coil-to-coil

TABLE I
EXPERIMENTAL WPT SYSTEM PARAMETERS

Symbol	Value	Unit
V_{DC}	0-600	V
t	1	μs
L_1	67.7	μH
C_1	52.2	nF
R_1	138	mΩ
L_2	67.5	μH
C_2	52.1	nF
R_2	142	mΩ
d	50-250	mm
R_{La}	5-25	Ω

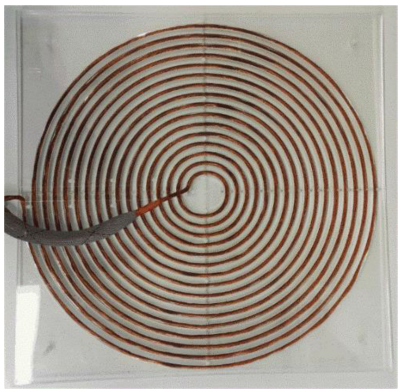

Fig. 12. Coil used in the experiments.

TABLE II
DESIGN PARAMETERS OF THE COILS

Coil design parameter	Value	Unit
Litz wire diameter	6	mm
Inner radius	30	mm
Outer radius	286	mm
Channel width	10	mm
Number of Coils	16	#

distance is determined. In the experiments, the coil-to-coil distance will vary from 50 to 250 mm to provide different coupling coefficients from strong coupling to weak coupling to trigger or suppress the FSP according to Fig. 2.

In this article, as the distance between the two coils needs to be tuned to provide different coupling coefficient from weak coupling to strong coupling in the analysis and experiments, the ferrite is not added for avoiding the changing of the self-inductance of the coils. Which can make sure that the system always operates at a resonate condition, and thereby providing a fair comparison when the power transfer distance varies. It should be noted that even though air coils are adopted in this article, the analysis about the FSP and the system control method by utilizing the FSP are both applicable to the coils with ferrite.

The experimental setup is shown in Fig. 13. A dc power supply EA-PS 81000-30 dc is used to supply power to the whole system. The primary-side coil system receives the desired high-frequency power excitation from the full bridge inverter which consists of SiC power MOSFETs S_1–S_4 (CREE. C2M0040120D), then the power is transmitted to the secondary side of the WPT system, lastly, the power will be delivered to the load resistors

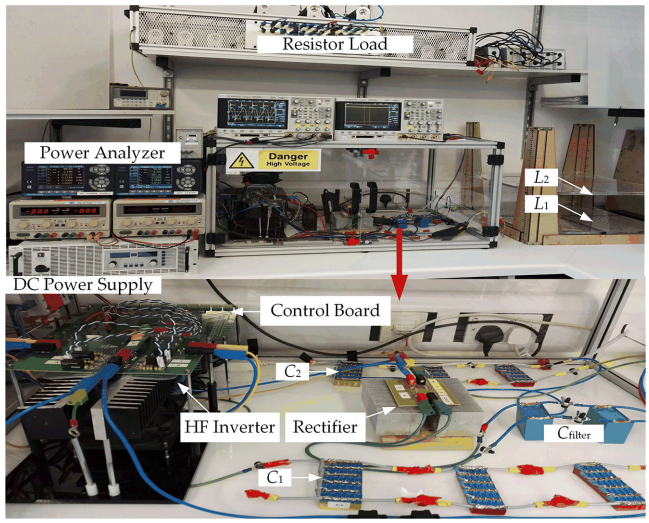

Fig. 13. Experimental platform of the WPT system.

after being rectified by an H-bridge rectifier made by four SiC diodes (CREE. C4D20120) to reduce losses. Two Fluke Norma 4000 power analyzers are used to measure the dc input power, inverter output power, rectifier input power, and the load power. 400 MHz passive probes (PMK, PHV 1000) are used to measure the gate-to-source voltage and drain-to-source voltage. Rogowski coil (CWTUM03B/1/80) is used to measure the drain current. Differential probe (Agilent, N2791A) is used to measure the output voltage of the inverter. 50 MHz current probe (Agilent, 1147A) is used to measure the output current of the inverter. 100 MHz oscilloscope (Agilent, MSO-X 3014A) is used to capture the voltage and current waveforms.

A. *Experiments for Constant Output Power Control Strategy*

To verify the effectiveness and advantages of the constant output power control method by utilizing the FSP, the coil-to-coil vertical distance is fixed at 150 mm first and the load resistance will vary from 5 to 25 Ω to provide different load conditions. And then, the load resistance will be kept constant at 15 Ω and the coil-to-coil vertical distance will increase from 50 to 250 mm to provide different coupling conditions. In this way, the FSP can occur first and be completely suppressed subsequently (see Fig. 2) to provide different system operating conditions.

Based on the calculation functions of Methods A and B, the desired 3.3 kW constant output power can both be effectively maintained with slight errors when the load resistance or the coupling coefficient varies in the WPT system, as shown in Figs. 14 and 15. The error is not only caused by these assumptions in the calculative process but also the non-negligible stray resistance in the leads and the connection nodes, particularly for the parasitic resistance in the screws used for connecting the components in the WPT system. But, it will not impact the analysis about the study of the constant output control methods and when the stray resistance existing in the leads and connection nodes can

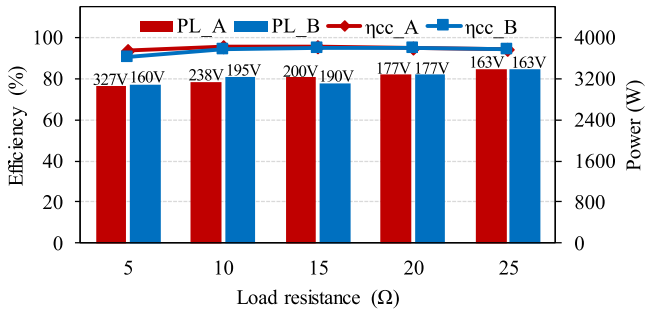

Fig. 14. Experimental results for constant output power when R_{La} varies.

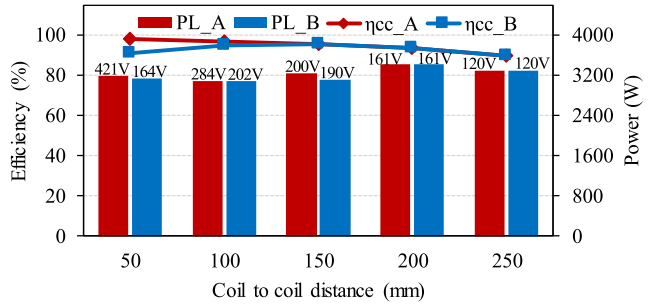

Fig. 15. Experimental results for constant output power when coil-to-coil distance varies.

be greatly reduced or precisely predicted, the precision can be further improved.

As can be seen from Fig. 14, when the load resistance increases from 5 to 25 Ω and the coil-to-coil distance is kept constant at 150 mm, the dc input voltage reduces from 327 to 163 V by adjusting the dc input voltage directly (Method A). While for Method B, when the FSP occurs, the dc input voltage can be greatly reduced compared to Method A, i.e., V_{DC} is reduced from 327 to 160 V at 5 Ω load resistance. Besides, it can be found out from the experimental results that the lower the load resistance is, the higher the required input dc voltage will be, and the dc input voltage can be greater reduced by Method B. With the load resistance continually increasing, the FSP disappears as expected, the desired driving frequency of Method B corresponding to the maximum output power point equals to resonant frequency. Therefore, Method B does not need to tune the driving frequency anymore and Method B is Method A essentially in this case. Regards to the power transfer efficiency, the efficiency derived by Method B cannot be higher than those with Method A with the same load resistance, because maximum efficiency can only be achieved when the driving frequency equals the resonant frequency. When the load resistance is kept constant and the coil-to-coil distance increases from 50 to 250 mm, similar results can be derived as the load resistance varies (see Fig. 15).

As a conclusion, compared with tuning the dc input voltage to adjust the output power, utilizing the frequency splitting characteristic of the WPT system can fully utilize the system power transfer capacity and can decrease the driving frequency/dc input voltage, which is beneficial in reducing the stress on the components used in the WPT system, thereby providing a safer operating condition for the system.

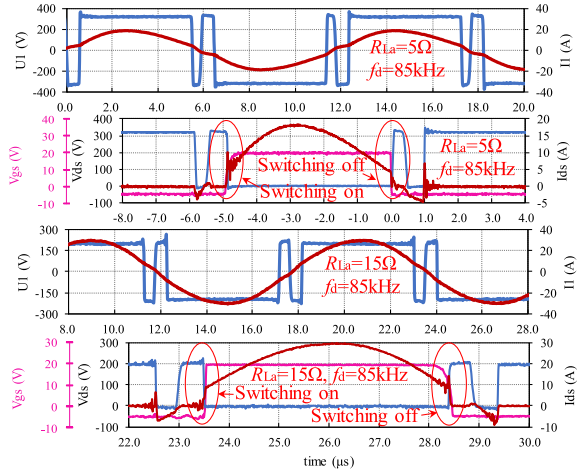

Fig. 16. Experimental waveforms of the WPT system in resonant conditions.

B. *Experiments for ZVS Implementation Strategy*

As analyzed in Section II, when the coil-to-coil distance is fixed at 150 mm, the FSP will occur at 5 Ω load resistance, and gradually disappears at 15 Ω load resistance (see Figs. 2 and 6). Therefore, these two load conditions are selected to validate that the ZVS realization method can be effectively achieved no matter the FSP occurs or not.

The experiment for exactly resonant condition ($f_{\mathrm{d}} = f_{\mathrm{r}}$) is carried out first. The dead-time of the driving signals for the full bridge dc–ac inverter is set to be 1 μs for safety in the experiments. The measured output voltage and current waveforms of the inverter and the switching waveforms of the MOSFET are shown in Fig. 16.

As can be seen from Fig. 16 that when the WPT system operates under resonant condition, the output voltage and current waveforms of the inverter show good consistency with the theoretical analysis, and that the SiC MOSFETs operate in hard switching conditions, which is also consistent with the analysis in Section II (see Fig. 7).

According to the theoretical calculation results presented in Section III-B, for realizing ZVS operation of the dc–ac inverter used in this 85 kHz WPT system and minimizing the impacts on the power transfer efficiency and amount, the desired driving frequencies are 78 and 75 kHz with a 5 Ω load, and 95 and 78 kHz with a 15 Ω load for inductive and capacitive input impedance, respectively.

The measured output and switching waveforms of the inverter and the MOSFET under these two load conditions are shown in Figs. 17 and 18 accordingly. It can be seen that with the ZVS realization methods, ZVS ON or OFF can be realized as desired by tuning the inverter input impedance to inductive or capacitive, respectively. The experimental waveforms show good consistency with the analysis in Section II about the analysis on the

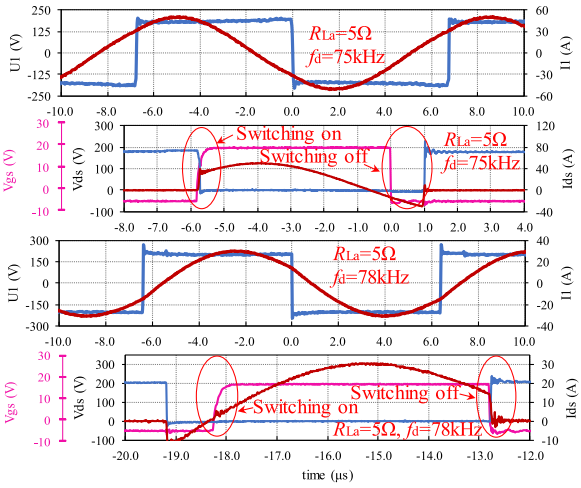

Fig. 17. Experimental waveforms of the 85 kHz WPT system in ZVS experiments with a 5 Ω load.

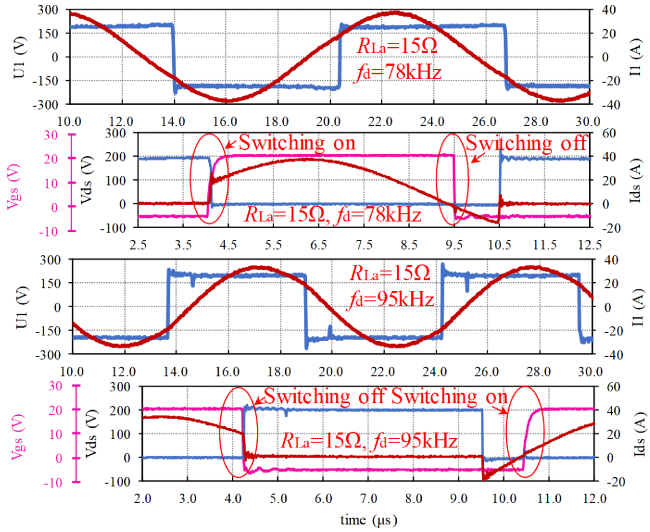

Fig. 18. Experimental waveforms of the 85 kHz WPT system in ZVS experiments with a 15 Ω load.

voltage and current waveforms of the dc–ac inverter affected by characteristic of the input impendence.

To analyze the impact of the proposed ZVS operation strategy on the performance of the WPT system, all the experimental results are presented in one figure as shown in Fig. 19. First, it can be found out that whether the WPT system operates at resonant condition or ZVS condition, the output power can all be maintained at 3.3 kW with the proposed system control method by utilizing the FSP. Second, with the proposed ZVS implementation method, the coil-to-coil efficiency decreases slightly because of the unresonant operating conditions, but the inverter efficiency is effectively improved, e.g., from 95% to 97% when the FSP occurs at 5 Ω load, and from 95% to 98% when the FSP disappears at 15 Ω load. Even though it results in a small decrease in the coil-to-coil efficiency, but higher inverter efficiency is critical for system safety, and can thereby reduce

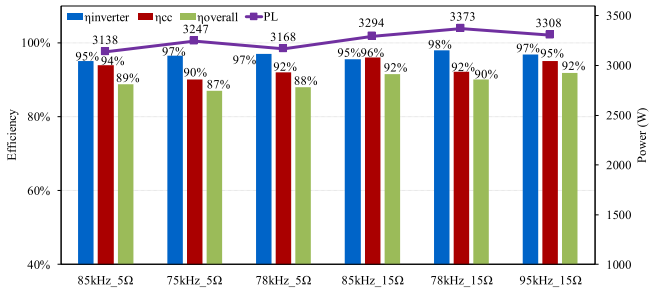

Fig. 19. System performance under different conditions.

the volume of the heatsink and increase the power density of the system. Besides, the overall efficiency of the whole system can be nearly maintained constant as the resonant conditions.

V. Conclusion

In this article, the FSP of the two-coil WPT system with an SS compensation topology is studied in detail. It is found in this article that the FSP will occur when the coupling coefficient increases or the load resistance decreases. As the FSP cannot be completely suppressed in a practical WPT system, a system control method by utilizing the advantages of the FSP is proposed in this article. With the proposed method, the FSP can help to decrease the dc input voltage and create ZVS operation of the dc–ac inverter with the same power transfer amount. An 85 kHz, 3.3 kW WPT system is built up to validate the proposed method. The experimental results show good consistency with the theoretical analysis. In the experiments, when the FSP occurs at 150 mm coil-to-coil distance and 5 Ω load resistance, the dc input voltage is reduced from 327 to 160 V with a 3.3 kW load power, meanwhile, ZVS of the dc–ac inverter is realized and the inverter efficiency is improved from 95% to 97%.

References

[1] Z. Zhang, K. T. Chau, C. Liu, F. Li, and T. W. Ching, "Quantitative analysis of mutual inductance for optimal wireless power transfer via magnetic resonant coupling," *IEEE Trans. Magn.*, vol. 50, no. 11, Nov. 2014, Art. no. 8600504.

[2] G. Tortora, F. Mulana, G. Ciuti, P. Dario, and A. Menciassi, "Inductive-based wireless power recharging system for an innovative endoscopic capsule," *Energies*, vol. 8, no. 9, pp. 10315–10334, Sep. 2015.

[3] S. Senjuti, "Design and optimization of efficient wireless power transfer links for implantable biotelemetry systems," Master's thesis, Univ. Western Ontario, London, ON, Canada, 2013, p. 97.

[4] R. F. Xue, K. W. Cheng, and M. Je, "High-efficiency wireless power transfer for biomedical implants by optimal resonant load transformation," *IEEE Trans. Circuits Syst. I, Reg. Papers*, vol. 60, no. 4, pp. 867–874, Apr. 2013.

[5] A. Shekhar, V. Prasanth, P. Bauer, and M. Bolech, "Economic viability study of an on-road wireless charging system with a generic driving range estimation method," *Energies*, vol. 9, no. 2, pp. 1–20, Feb. 2016.

[6] Y. Gao, K. B. Farley, and Z. T. H. Tse, "A uniform voltage gain control for alignment robustness in wireless EV charging," *Energies*, vol. 8, no. 8, pp. 8355–8370, Aug. 2015.

[7] U. K. Madawala and D. J. Thrimawithana, "A bidirectional inductive power interface for electric vehicles in V2G systems," *IEEE Trans. Ind. Electron.*, vol. 58, no. 10, pp. 4789–4796, Oct. 2011.

[8] J. Shin *et al.*, "Design and implementation of shaped magnetic-resonance-based wireless power transfer system for roadway-powered moving electric vehicles," *IEEE Trans. Ind. Electron.*, vol. 61, no. 3, pp. 1179–1192, Mar. 2014.
[9] H. Hoang, S. Lee, Y. Kim, Y. Choi, and F. Bien, "An adaptive technique to improve wireless power transfer for consumer electronics," *IEEE Trans. Consum. Electron.*, vol. 58, no. 2, pp. 327–332, May 2012.
[10] J. C. Lin, "Wireless power transfer for mobile applications, and health effects [Telecommunications Health and Safety]," *IEEE Antennas Propag. Mag.*, vol. 55, no. 2, pp. 250–253, Apr. 2013.
[11] G. A. Covic, G. Elliott, O. H. Stielau, R. M. Green, and J. T. Boys, "The design of a contact-less energy transfer system for a people mover system," in *Proc. Int. Conf. Power Syst. Technol. Proc.*, 2000, pp. 79–84.
[12] W. Niu, J. Chu, W. Gu, and A. Shen, "Exact analysis of frequency splitting phenomena of contactless power transfer systems," *IEEE Trans. Circuits Syst. I, Reg. Papers*, vol. 60, no. 6, pp. 1670–1677, Jun. 2013.
[13] J. Chu, W. Gu, W. Niu, and A. Shen, "Frequency splitting patterns in wireless power relay transfer," *IET Circuits, Devices Syst.*, vol. 8, no. 6, pp. 561–567, Nov. 2014.
[14] R. Huang, B. Zhang, D. Qiu, and Y. Zhang, "Frequency splitting phenomena of magnetic resonant coupling wireless power transfer," *IEEE Trans. Magn.*, vol. 50, no. 11, Nov. 2014, Art. no. 8600204.
[15] Y. Zhang and Z. Zhao, "Frequency splitting analysis of two-coil resonant wireless power transfer," *IEEE Antennas Wireless Propag. Lett.*, vol. 13, pp. 400–402, 2014.
[16] R. Huang and B. Zhang, "Frequency, impedance characteristics and HF converters of two-coil and four-coil wireless power transfer," *IEEE J. Emerg. Sel. Topics Power Electron.*, vol. 3, no. 1, pp. 177–183, Mar. 2015.
[17] M. Iordache, D. Niculae, L. I. Bobaru, and L. Mandache, "Circuit analysis of frequency splitting phenomena in wireless power transfer systems," in *Proc. 9th Int. Symp. Adv. Top. Elect. Eng.*, 2015, pp. 146–151.
[18] M. Iordache, L. Mandache, D. Niculae, and L. Iordache, "On exact circuit analysis of frequency splitting and bifurcation phenomena in wireless power transfer systems," in *Proc. Int. Symp. Signals, Circuits Syst.*, 2015, pp. 1–4.
[19] Y. Lyu *et al.*, "A method of using nonidentical resonant coils for frequency splitting elimination in wireless power transfer," *IEEE Trans. Power Electron.*, vol. 30, no. 11, pp. 6097–6107, Nov. 2015.
[20] S. Huang, Z. Li, and K. Lu, "Frequency splitting suppression method for four-coil wireless power transfer system," *IET Power Electron.*, vol. 9, no. 15, pp. 2859–2864, Dec. 2016.
[21] Y. Zhang, Z. Zhao, and K. Chen, "Frequency-splitting analysis of four-coil resonant wireless power transfer," *IEEE Trans. Ind. Electron.*, vol. 50, no. 4, pp. 2436–2445, Jul./Aug. 2014.
[22] R. Narayanamoorthi, A. V. Juliet, and B. Chokkalingam, "Frequency splitting-based wireless power transfer and simultaneous propulsion generation to multiple micro-robots," *IEEE Sens. J.*, vol. 18, no. 13, pp. 5566–5575, Jul. 2018.
[23] X. Liu, L. Clare, X. Yuan, C. Wang, and J. Liu, "A design method for making an LCC compensation two-coil wireless power transfer system more energy efficient than an SS counterpart," *Energies*, vol. 10, no. 9, pp. 1–28, Sep. 2017.
[24] X. Liu, C. Xia, and X. Yuan, "Study of the circular flat spiral coil structure effect on wireless power transfer system performance," *Energies*, vol. 11, no. 11, pp. 1–21, Oct. 2018.

Xu Liu received the B.S. degree in electronic science and technology and the Ph.D. degree in electrical engineering from the China University of Mining and Technology, Xuzhou, China, in 2012 and 2018, respectively.

From 2015 to 2017, he was a Joint Ph.D. Student with the University of Bristol, Bristol, U.K. Since 2018, he has been a Research Associate with the School of Electrical and Power Engineering, China University of Mining and Technology. His current research interests include wireless power transfer technology and advanced power semiconductors.

Xibo Yuan (Senior Member, IEEE) received the B.S. degree from China University of Mining and Technology, Xuzhou, China, in 2005, and the Ph.D. degree from Tsinghua University, Beijing, China, in 2010, both in electrical engineering.

Since 2017, he has been a Professor in the Electrical Energy Management Group, Department of Electrical and Electronic Engineering, University of Bristol, Bristol, U.K, where he became a Lecturer in 2011, a Senior Lecturer in 2015, and a Reader in 2016. His research interests include power electronics and motor drives, wind power generation, multilevel converters, application of wide-bandgap devices, electric vehicles, and more electric aircraft technologies.

Prof. Yuan is an Associate Editor of IEEE TRANSACTIONS ON INDUSTRY APPLICATIONS and IEEE JOURNAL OF EMERGING AND SELECTED TOPICS IN POWER ELECTRONICS. He is a fellow of IET and was a recipient of The Isao Takahashi Power Electronics Award in 2018. He also holds the Royal Academy of Engineering/Safran Chair in Advanced Aircraft Power Generation Systems. He is an Executive Committee Member of the UK National Centre for Power Electronics and the IET Power Electronics, Machines and Drives (PEMD) network.

Chenyang Xia received the B.S., M.S., and Ph.D. degrees in control theory and control engineering from Chongqing University, Chongqing, China, in 2006, 2008, and 2010, respectively.

From 2018 to 2019, he was an Academic Visitor with the University of Auckland, New Zealand. He is currently a Professor with the School of Electrical and Power Engineering, China University of Mining and Technology, Xuzhou, China. His current research interests include wireless power transfer technology, power electronics, intrinsic safety switch power supply, and intelligent control.

Xiaojie Wu received the B.S. degree in industrial automation, and the M.S. and Ph.D. degrees in power electronics and power drives from the China University of Mining and Technology, Xuzhou, China, in 1988, 1991, and 2001, respectively.

From 2002 to 2004, he was a Postdoctoral Research Fellow with Tsinghua University, Beijing, China. Since 1991, he has been with the China University of Mining and Technology, where he is currently a Professor. He has authored or coauthored one book and more than 60 technical papers published in journals and conferences. His research interests include advanced control of electrical drives, multilevel converters, renewable energy generation systems, and power electronics.